Eur. Phys. J. B **18**, 39–47 (2000)

**THE EUROPEAN PHYSICAL JOURNAL B**

EDP Sciences


# Triangular antiferromagnetic order in the honeycomb layer lattice of $ErCl_3$

K.W. Krämer[1,a], H.U. Güdel[1], P. Fischer[2], F. Fauth[3], M.T. Fernandez-Diaz[3], and T. Hauß[4]

[1] Department for Chemistry and Biochemistry, University of Bern, Freiestrasse 3, 3000 Bern 9, Switzerland
[2] Laboratory for Neutron Scattering, Paul Scherrer Institute and ETH Zürich, 5232 Villigen PSI, Switzerland
[3] Institut Laue-Langevin, BP 156, 38042 Grenoble Cedex 9, France
[4] Hahn-Meitner Institute, Glienicker Strasse 100, 14109 Berlin, Germany

Received 1 December 1999 and Received in final form 21 July 2000

**Abstract.** $ErCl_3$ crystallizes in the $AlCl_3$-type layer structure. The crystal structure was refined in the paramagnetic state by powder neutron diffraction. The monoclinic lattice parameters at 1.5 K are $a$ = 6.8040(3) Å, $b$ = 11.7456(5) Å, $c$ = 6.3187(3) Å and $\beta$ = 110.851(3)°. The space group is C2/m. Short-range, predominantly in-plane, magnetic ordering occurs above 350 mK up to several Kelvin. Below $T_N$ = 350(5) mK a three-dimensional antiferromagnetic order with a propagation vector of $\mathbf{k} = (2/3, 0, -1/12)$ sets in. The magnetic structure of $ErCl_3$ was determined by powder and single-crystal neutron diffraction at temperatures down to 45 mK. The $Er^{3+}$ ions are located on two-dimensional honeycomb layers in the $a$-$b$ plane. There are two antiferromagnetically coupled 120° triangular sublattices which form right- and left-handed helices along the $c$-axis. The magnetic moments are oriented in the $a$-$b$ plane and amount to 3.3(1) $\mu_B/Er^{3+}$ at saturation. From the temperature dependence of the integrated neutron magnetic peak intensity a critical exponent $\beta$ = 0.23(2) was derived for the magnetic phase transition.

**PACS.** 75.25.+z Spin arrangements in magnetically ordered materials (including neutron and spin-polarized electron studies, synchrotron-source x-ray scattering, etc.) – 75.40.-s Critical-point effects, specific heats, short-range order – 61.12.Ld Single-crystal and powder diffraction

## 1 Introduction

The rare-earth trihalides $MX_3$ are an interesting family of compounds to study the magnetic interactions of the rare-earth ions in an insulating lattice. They offer the possibility to exchange the magnetic cations $M^{3+}$ (Ce – Yb) as well as the anions $X^-$ (F – I) in systematic ways in order to investigate correlations between chemical composition, structure and magnetic behavior. Due to the shielding of the $4f$ electrons the exchange interactions are weak and comparable in magnitude to the magnetic dipole interactions. The trihalides of the heavier lanthanides crystallize in layer-type structures which are isostructural to $AlCl_3$ for $MCl_3$ with M = Dy – Lu and to $BiI_3$ for $MBr_3$ with M = Gd – Lu and also $MI_3$ with M = Sm – Lu. The materials are very hygroscopic, which complicates their preparation and handling. In addition, the low magnetic ordering temperatures, usually below 1 K, are only accessible in dilution cryostats. Magnetic susceptibility data down to the ordering temperatures have been published for $ErCl_3$ [1], $HoCl_3$ [2] and $GdBr_3$ [3]. From these data a ferromagnetic or canted-antiferromagnetic order with a net moment and $T_c$ = 307 mK was deduced for $ErCl_3$ [1]. In contrast to this we determined a purely antiferromagnetic order. Clearly, neutron diffraction is the method of choice for a reliable magnetic structure determination.

This work is part of a systematic study of the magnetic ordering phenomena within the series $ErX_3$ (X = F, Cl, Br, I) by magnetic neutron diffraction. In this series the heavier halides from X = Cl to I have closely related layer structures, and they have common features in their magnetic ordering. A comparison of their properties has very recently been reported in a short communication [4]. Here we provide a detailed account of the magnetic order in $ErCl_3$. The properties of $ErF_3$ were reported earlier [5].

## 2 Experiment

$ErCl_3$ was prepared from $Er_2O_3$ (Alfa, 99.9%), $NH_4Cl$ (Merck, 99.8%) and HCl (Merck, p.a.) according to the $NH_4Cl$-route [6] and sublimed in a silica apparatus under vacuum for purification. The insulating, ionic compound forms transparent, pink, plate-like crystals. Single crystals were grown in silica ampoules by the vertical Bridgman technique with a moving furnace. Due to the hygroscopicity of $ErCl_3$ all handling was done in nitrogen-filled glove boxes ($H_2O$ < 0.1 ppm).

[a] e-mail: karl.kraemer@iac.unibe.ch

**Table 1.** Crystallographic data of $ErCl_3$ at 1.5 K in the paramagnetic state determined by powder neutron diffraction. Space group: C2/m (No. 12). Lattice parameters: $a$ = 6.8040(3) Å, $b$ = 11.7456(5) Å, $c$ = 6.3187(3) Å, $\beta$ = 110.851(3)°. Number of fitted parameters: 21. Number of reflections: 289 for $\lambda = 1.9079$ Å and $2\theta = 10° - 159°$. $R_{\rm wp}$ : 4.5%, $R_{\rm exp}$ : 3.2%, $\chi^2 = 2.0$, $R_{\rm inuc} = 4.6\%$.

| atom | site | $x/a$ | $y/b$ | $z/c$ | $B$ / Å$^2$ |
|---|---|---|---|---|---|
| Er | $4g$ | 0 | 0.1662(3) | 0 | 0.12(4) |
| Cl1 | $4i$ | 0.2199(5) | 0 | 0.2475(6) | 0.60(2) |
| Cl2 | $8j$ | 0.2411(4) | 0.1776(1) | 0.7537(4) | |

The crystal structure of $ErCl_3$ was refined from a powder neutron-diffraction measurement at 1.5 K in the paramagnetic state. The measurement was done at the D1A diffractometer of the Institute Laue-Langevin (ILL), Grenoble, France. The sample was sealed in a vanadium container ($\phi$ 8 × 50 mm$^3$) under helium atmosphere and cooled in a helium cryostat. The neutron wavelength was $\lambda = 1.9079$ Å.

The magnetic structure of $ErCl_3$ was determined from a powder neutron measurement at the D1B diffractometer of the ILL at a wavelength of $\lambda = 2.5169$ Å. The sample was filled in a copper container and cooled by a bottom-loading ILL dilution cryostat down to 60 mK. To ensure a good thermalization of the sample, the powder was mechanically compressed and $^4$He gas condensed into the sample container *via* a capillary.

The **k**-vector and the temperature dependence of the ordered magnetic moment per $Er^{3+}$ were determined from a single-crystal neutron experiment at the V1 diffractometer of the Hahn-Meitner Institute (HMI), Berlin, Germany, at a neutron wavelength of $\lambda = 4.623$ Å using a 20 × 20 cm$^2$ area detector. A single crystal of 15 × 13 × 3 mm$^3$ size was selected under an optical microscope in a dry box and its orientation determined between crossed polarizers. The crystal was glued onto a copper block and sealed under helium atmosphere into a copper container filled with copper powder. The crystal was cooled down to 45 mK with a dilution stick inserted in an ILL-type helium cryostat.

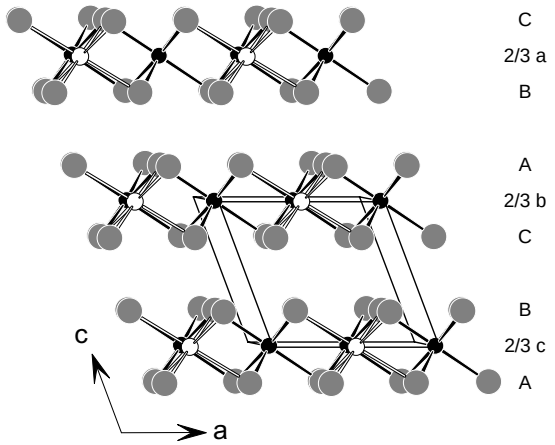


**Fig. 1.** Perspective view of the $ErCl_3$ structure along the $b$-axis. Black spheres denote $Er^{3+}$ ions, gray spheres $Cl^-$ ions, and empty spheres octahedral voids in the Er layer. The layer stacking sequence is indicated at the right hand side according to a cubic closest packing of $Cl^-$ ions with $Er^{3+}$ ions occupying 2/3 of the octahedral voids of every other layer in an ordered way.

## 3 Results

### 3.1 Crystal structure

$ErCl_3$ crystallizes in the $AlCl_3$-type structure with the monoclinic space group C2/m and 4 formulas per unit cell [7]. The crystallographic data were refined from a powder neutron-diffraction measurement at 1.5 K in the paramagnetic state by the Rietveld method using the program FULLPROF [8]. The relevant model parameters obtained from the best fit to the data between $2\theta = 10° - 159°$ for $\lambda = 1.9079$ Å are summarized in Table 1. For space group C2/m 289 possible reflections fall into this $2\theta$ range. Refining a total of 21 parameters, the fit yields agreement factors of $R_{\rm wp} = 4.5\%$, $R_{\rm exp} = 3.2\%$, and $\chi^2 = 2.0$ for the profile and $R_{\rm inuc} = 4.6\%$ for the integrated intensities. The definitions of the statistical parameters are given in the equations (1–4). A Thompson-Cox-Hastings pseudo-Voigt peak shape was used and data were corrected for absorption based on a measured value of $\mu \times r = 0.4215$ at $\lambda = 1.9079$ Å. The powder showed a preferred orientation along [001]. A perspective view of the crystal structure along the $b$-axis and a projection onto the $a$-$b$ plane are shown in Figures 1 and 2, respectively. Important interatomic distances and angles are given in Table 2.

$$R_{\rm wp} = 100\Big(\sum_i w_i|y_{oi} - y_{ci}|^2 / \sum_i w_i|y_{oi}|^2\Big)^{1/2} \quad (1)$$

$$R_{\rm exp} = 100\Big[(N - P + C)/\sum_i w_i y_{oi}^2\Big]^{1/2} \quad (2)$$

$$\chi^2 = (R_{\rm wp}/R_{\rm exp})^2 \quad (3)$$

$$R_{\rm inuc} = 100\sum_i |I_{oi} - I_{ci}|/\sum_i |I_{oi}|. \quad (4)$$

### 3.2 Magnetic structure

The magnetic structure of $ErCl_3$ was determined by neutron diffraction. A powder sample was measured on the D1B diffractometer at the ILL and a single crystal on the V1 diffractometer at the HMI. Upon cooling additional magnetic Bragg peaks were observed which could not be indexed in terms of the crystallographic cell. In order to extract the magnetic contributions from the measured neutron-diffraction patterns a difference diagram for 60–485 mK was calculated, see Figure 3. In the single-crystal measurement significant intensity variations were observed for equivalent magnetic Bragg peaks, because of the strong absorption at $\lambda = 4.6$ Å and effects due

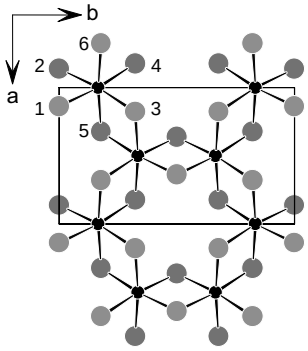


**Fig. 2.** View onto an $ErCl_3$ honeycomb layer. Black spheres denote $Er^{3+}$ ions and gray spheres $Cl^-$ ions. The numbering of the $Cl^-$ ions refers to Table 2.

**Table 2.** Interatomic distances and angles in $ErCl_3$ at 1.5 K. Coordination numbers: Er = 6 (Cl), Cl = 2 (Er) + 12 (Cl).

| atoms | distances / Å | atoms | distances / Å |
|---|---|---|---|
| Er-Er | 3.904 (intralayer) | Er-Cl1 | $2 \times 2.613$ |
| | $2 \times 3.931$ (intralayer) | Er-Cl2 | $2 \times 2.634$ |
| | | | $2 \times 2.636$ |
| | $2 \times 6.319$ (interlayer) | | |
| | $2 \times 6.330$ (interlayer) | Cl-Cl | 3.475–4.221 |

Cl-Er-Cl angles of the $ErCl_6$ octahedra. The numbers of the chlorine atoms refer to Figure 2: 1–2 = Cl1, 3–6 = Cl2. Intralayer Er-Er-Er angles: 119.89°, $2 \times 120.06°$.

| atoms | | angle / ° |
|---|---|---|
| 1-Er-2 | | 83.34 |
| 1-Er-3 | 2-Er-4 | 92.68 |
| 1-Er-4 | 2-Er-3 | 173.62 |
| 1-Er-5 | 2-Er-6 | 92.71 |
| 1-Er-6 | 2-Er-5 | 91.64 |
| 3-Er-4 | | 91.71 |
| 3-Er-5 | 4-Er-6 | 83.55 |
| 3-Er-6 | 4-Er-5 | 92.39 |
| 5-Er-6 | | 174.18 |

to the crystal shape. It was impossible to correct the intensity data for these effects to a sufficient accuracy. Thus the powder data were used for the determination of the magnetic structure and the magnitude of the ordered magnetic moment per $Er^{3+}$.

From a pattern matching of the powder data and especially from the single crystal measurement the propagation vector of $\mathbf{k} = (2/3,\, 0,\, -1/12)$ was determined. The propagation vector is given with respect to the C-centered crystallographic unit cell to avoid the transformation to a primitive, triclinic cell. The small component of the **k**-vector along the *c*-axis is evident from the positions of the single crystal reflections, see Figure 4. The positions of the magnetic reflections do not shift with temperature, and we thus have no evidence that the magnetic structure is not commensurate.

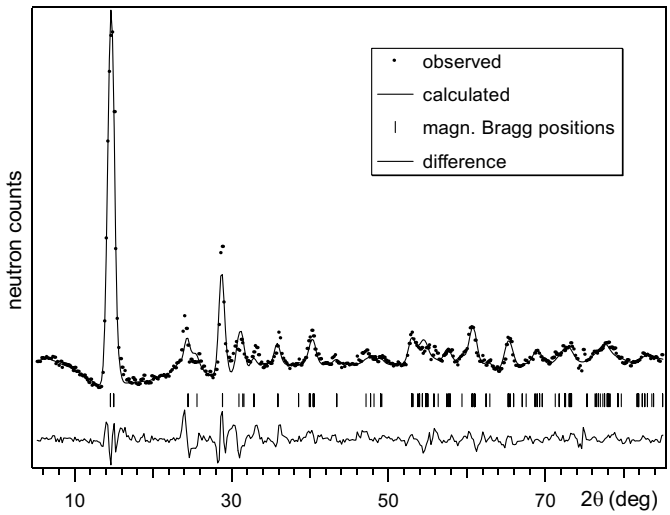


**Fig. 3.** Powder neutron diffraction difference diagram of $ErCl_3$ for 60–485 mK and $\lambda = 2.5$ Å. The pattern shows the contributions due to magnetic diffraction. The full lines correspond to the best Rietveld fit.

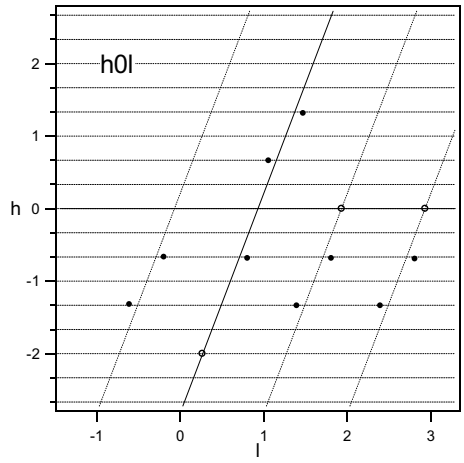


**Fig. 4.** Bragg peak positions in the $h0l$ plane detected by neutron diffraction from a single crystal of $ErCl_3$ at 45 mK. The positions of the magnetic peaks (full circles) are defined by the **k**-vector (2/3,0,–1/12). Some nuclear peaks (open circles) are shown for reference. The position error is smaller than the size of the symbols.

The temperature dependence of the ordered magnetic moment per $Er^{3+}$ is shown in Figure 5. It corresponds to the square root of the normalized magnetic peak intensity, which was determined from the two strongest magnetic Bragg peaks of the powder pattern, *i.e.* $(2/3, 0, -1/12)$ and $(1/3, 1, 1/12)$ near $2\theta = 15°$, see Figure 3, as well as the $(-2/3, 0, 1/12)$ reflection in the single crystal measurement, see Figure 6. The Néel temperature is $T_N = 350(5)$ mK and saturation of the magnetic moment is achieved below 200 mK. The best fit of equation (5) to the single crystal data is shown as a line in Figure 5 and yields a critical exponent of $\beta = 0.23(2)$.

$$M/M_0 = (1 - T/T_N)^{\beta}. \qquad (5)$$

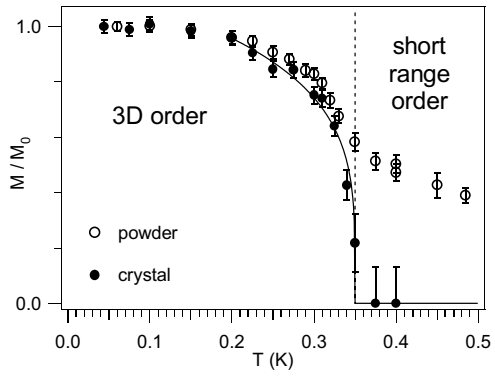


**Fig. 5.** Temperature dependence of the ordered magnetic moment of $ErCl_3$ determined from integrated magnetic peak intensities by neutron diffraction. Open symbols were determined from the intensity of the strongest powder peak at $2\theta = 15°$ and full symbols from the (–2/3, 0, 1/12) single crystal reflection. The line shows the best fit of equation (5) to the single crystal data which yields the critical exponent $\beta = 0.23(2)$.

The crystallographic unit cell contains 4 $Er^{3+}$ ions on the site ($4g$) of space group C2/m. Their coordinates are $0, y, 0$, $0, -y, 0$, $1/2, 1/2+y, 0$ and $1/2, 1/2-y, 0$. From $0, y, 0$ the second position $0, -y, 0$ is generated by a mirror plane perpendicular to the $b$-axis as well as by a center of inversion at the origin. The remaining 2 positions are generated by the translation $(1/2, 1/2, 0)+$, *i.e.* the C-centering. The magnetic Bragg peaks are satellites of the nuclear ones and can be indexed as $hkl + / - \mathbf{k}$. The positions of the magnetic peaks are marked in Figure 3. They obey the C-centering extinction rule: $hkl$ with $h + k = 2n$ only, with $n$ being an integer number. No further peaks occur. Thus the C-centering of the nuclear lattice persists in the magnetically ordered state, and only two magnetic sublattices, related to $0, y, 0$ and $0, -y, 0$, have to be considered for the description of the magnetic structure. The orientations of the magnetic moments at the $1/2, 1/2+y, 0$ and $1/2, 1/2-y, 0$ positions are correlated to those at $0, y, 0$ and $0, -y, 0$, respectively, by the **k**-vector [9]. The ($4g$) site symmetry is .2., *i.e.* the atoms are situated on 2-fold axes parallel to the $b$-axis. This restricts the orientation of the magnetic moments to be parallel or perpendicular to the $b$-axis. Magnetic moments transform as axial vectors [10]. According to group theory, four possible configurations result [11] which are summarized in Table 3. Calculations for all four configurations were performed with the program FULLPROF, and the best results were obtained for $A_g$ and $B_u$. However, no single mode model could reproduce the observed pattern satisfyingly, because they yield intensity for only one of the strong, close-lying (2/3, 0, –1/12) and (1/3, 1, 1/12) magnetic peaks near $2\theta = 15°$. Accordingly, dual mode models were tested and the $A_g + B_u$ one was found to reproduce the observed intensities. Its coupling scheme is $(\mu_x, \mu_y, \mu_z)$ for the position $0, y, 0$ and $(-\mu_x, \mu_y, -\mu_z)$ for the position $0, -y, 0$.

In Figure 3 the result of the best fit of 5 parameters, *i.e.* magnetic moment, zero-point, half-width, asymmetry,

**Table 3.** Possible coupling schemes of the magnetic moments for site ($4g$) in space group C2/m, point symmetry $C_2$.

| position | $A_g$ | $B_g$ | $A_u$ | $B_u$ |
|---|---|---|---|---|
| $0, y, 0$ | $(0, \mu_y, 0)$ | $(\mu_x, 0, \mu_z)$ | $(0, \mu_y, 0)$ | $(\mu_x, 0, \mu_z)$ |
| $0, -y, 0$ | $(0, \mu_y, 0)$ | $(\mu_x, 0, \mu_z)$ | $(0, -\mu_y, 0)$ | $(-\mu_x, 0, -\mu_z)$ |

**Table 4.** Magnetic structure of $ErCl_3$. $\mu_0 = 3.3(1)\mu_B$ per $Er^{3+}$ at saturation; $\mathbf{k} = (2/3, 0, –1/12)$; $\varphi = (2/3 \times t_x - 1/12 \times t_z)360°$.

| magnetic sublattice | coupling scheme | magnetic moment |
|---|---|---|
| $0, y, 0$ | $\begin{pmatrix} \mu_x \\ \mu_y \\ \mu_z \end{pmatrix}$ | $\mu/\mu_0 = \begin{pmatrix} \cos\varphi \\ \sin\varphi \\ 0 \end{pmatrix}$ |
| $0, -y, 0$ | $\begin{pmatrix} -\mu_x \\ \mu_y \\ -\mu_z \end{pmatrix}$ | $\mu/\mu_0 = \begin{pmatrix} \cos(180° - \varphi) \\ \sin(180° - \varphi) \\ 0 \end{pmatrix}$ |

and preferred orientation along [001], is shown. It yields a magnetic moment for $Er^{3+}$ of $\mu_0 = 3.3(1)\mu_B$ at saturation and agreement factors of $R_{wp} = 11.5\%$, $R_{exp} = 4.3\%$, $\chi^2 = 7.3$ and $R_{imag} = 9.9\%$. $R_{imag}$ is defined analogous to $R_{inuc}$ in equation (4). The structural parameters for this fit were taken from the refinement at 1.5 K and kept fixed in order to reduce the number of variables. The rather general **k**-vector (2/3, 0, –1/12) suggests a sine modulated or a helical magnetic structure [12]. For $ErCl_3$ the best agreement between observed and calculated magnetic neutron intensities was obtained for a helical configuration with magnetic moments in the $a$-$b$ plane and an equal amplitude $\mu_0$ for $\mu_x$ and $\mu_y$, *i.e.* $\mu_x = \mu_0 \cos\varphi$, $\mu_y = \mu_0 \sin\varphi$, and $\mu_z = 0$, see Table 4. $\varphi$ is the phase factor, which is defined as the scalar product of the **k**-vector and the position vector of the respective $Er^{3+}$ ion. The position vector $(t_x, t_y, t_z)$ is the sum of the position vector $(x, y, z)$ within the unit cell and the translation vector $\tau$. According to the $A_g + B_u$ coupling scheme given above, the orientation for those $Er^{3+}$ ions which belong to the 0, $y$, 0 magnetic sublattice is correlated to $\varphi$, whereas the orientation for the $0, -y, 0$ sublattice corresponds to $(180° - \varphi)$, see Table 4. It was found that the absolute value of the phase factor $\varphi$ cannot be determined. Because the two sublattices behave as interlocked right- and left-handed helices, their magnetic diffraction contributions cancel for $\mu_x$ and add up for $\mu_y$. For any angle the same powder and single crystal diffraction pattern is obtained.

## 4 Discussion

### 4.1 Crystal structure

The most characteristic structural feature of $ErCl_3$ is its layer structure. According to the Niggli formula $ErCl_{6/2}$

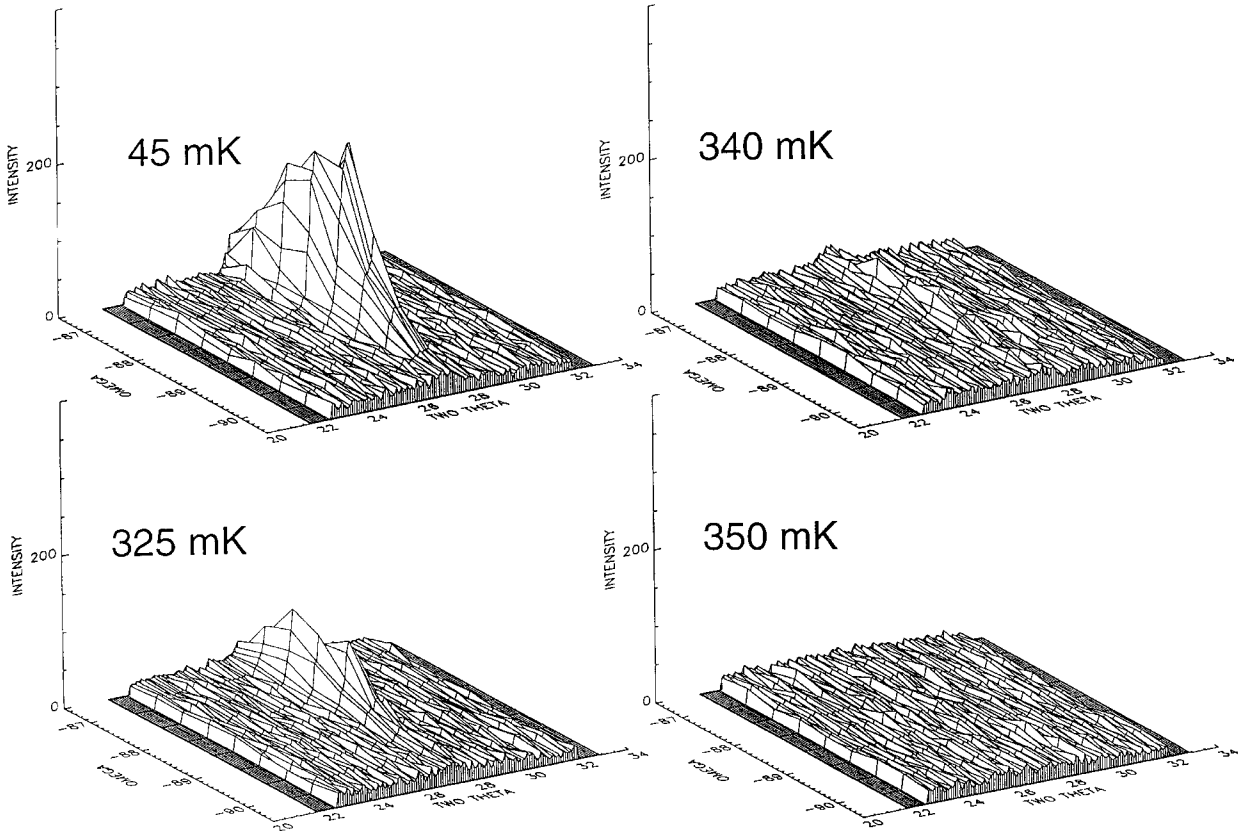


**Fig. 6.** Rocking curves ($\omega$-$2\theta$ plots) of the (–2/3, 0, 1/12) single-crystal magnetic reflection for $\lambda = 4.6$ Å measured by neutron diffraction at 45 mK and close to the 3D magnetic ordering temperature $T_N = 350(5)$ mK.

each $Er^{3+}$ ion is surrounded by 6 $Cl^-$ ions in the geometry of a distorted octahedron. Each octahedron is linked *via* three common edges to neighboring ones, leading to layers parallel to the *a*-*b* plane as shown in Figure 2. The layers are stacked along the *c*-axis, as shown in Figure 1, and hold together by van-der-Waals forces. This pronounced anisotropy governs the physical properties of $ErCl_3$. The crystals cleave easily parallel to the *a*-*b* plane and are rather soft. On bending they do not break and behave like a stack of paper in which the single sheets can move relative to each other. The layer structure also determines the magnetic properties, as will be discussed below. For the understanding of the properties of $ErCl_3$ as well as a comparison with the heavier erbium halides, $ErBr_3$ and $ErI_3$, a description of the structure in terms of a closest packing of spheres is useful. The $ErCl_3$ structure can be derived from a cubic closest packing of $Cl^-$ ions. The $Er^{3+}$ ions occupy 2/3 of the octahedral voids of every other layer in an ordered way. This results in the motif ...*A*,2/3 *c*, *B*, *C*,2/3 *b*, *A*, *B*, 2/3 *a*, *C*... for the layer stacking along the *c*-axis, where the capital letters *A*, *B*, *C* denote the $Cl^-$ layers and $a, b, c$ the $Er^{3+}$ layers. For clarity, the unoccupied positions in the Er layers are marked by open spheres in Figure 1. Due to these unoccupied positions located at $1/2, 0, 0$ and $0, 1/2, 0$, see Figure 2, the $Er^{3+}$ ions form two-dimensional (2D) honeycomb layers in which each erbium has three neighbors at distances of 3.904 Å and 2×3.931 Å, see Table 2. The in-plane angles between the $Er^{3+}$ ions are 119.89° and 2 × 120.06°. Thus the $Er^{3+}$ ions exhibit an almost undistorted honeycomb net with respect to their distances and especially to their angles. For the chloride ions on the other hand, there are obvious deviations from an undistorted packing of spheres for which their positions would be $0.2452, 0, 0.25$ for Cl1 and $0.2548, 0.1667, 0.75$ for Cl2, *cf*. Table 1. Each $Cl^-$ ion coordinates two $Er^{3+}$ ions and one octahedral void, see Figure 2. As the result the Coulomb attraction shifts them towards the $Er^{3+}$ ions, which in turn elongates the Er-Er distances and leads to a widening of the structure in the *a*-*b* plane. This effect is also visible in the Cl-Er-Cl angles of the $ErCl_6$ octahedra which are close to 83.5° and 92° for the bridging and non-bridging edges, respectively, see Table 2. Along the *c*-axis the deviations from an undistorted packing are small. The Cl-Cl interlayer distances perpendicular to the *a*-*b* plane are 2.913 Å and 2.991 Å for layer pairs with and without $Er^{3+}$ ions in between, respectively. The lattice parameters at 1.5 K (Tab. 1) are in good agreement with those determined by X-ray diffraction at room temperature in reference [7] and in the more recent reference [13]. The thermal contraction between 295 K and 1.5 K amounts to 0.1%, 0.4% and 1.1% for the *a*-, *b*- and *c*-axis, respectively, and reflects the anisotropy of the lattice. The weak van-der-Waals bonds between the layers show the strongest compression upon cooling.

### 4.2 Magnetic structure

The magnetic properties of $ErCl_3$ are governed by the honeycomb layer structure of the $Er^{3+}$ ions and their single-ion anisotropy which is determined by the crystal field. A honeycomb layer can be derived from a triangular layer, *i.e.* a two-dimensional closest packing, by splitting it up into three triangular sublattices and leaving one sublattice unoccupied. The lattice constants of these sublattices are elongated by $\sqrt{3}$ and their axes rotated by 30° with respect to the original lattice. $ErCl_3$ shows a novel type of magnetic structure for a honeycomb lattice. The magnetic moments are oriented within the *a*-*b* plane and form two sublattices which both are 120° antiferromagnetic triangular nets. The orientation of the magnetic moments depends on the angles $\varphi$ and $(180° - \varphi)$ for the two sublattices, respectively, where $\varphi$ is the phase factor, see Table 4. Those moments related to $\varphi$ show a right-handed rotation along the **k**-vector. The rotation axis is perpendicular to the *a*-*b* plane, *i.e.* parallel to the reciprocal $c^*$-axis. The ions which belong to this first sublattice are denoted by the open symbols in Figure 7. The second sublattice is related to $(180° - \varphi)$ and denoted by full symbols. It shows a left-handed rotation along the **k**-vector. The absolute orientation of the magnetic moments in the *a*-*b* plane cannot be fixed. There is an infinite rotational degree of freedom and regardless of the in-plane rotation angle the diffraction patterns are identical. But the two sublattices are interlocked like a system of gear wheels with their axes placed on the honeycomb-lattice points and oriented perpendicular to the layer. Each wheel is in touch with its three neighbors belonging to the other sublattice. Turning the first gear wheel clockwise forces its three neighbors to turn counter-clockwise about the same angle. The six next-nearest neighbors which belong to the same sublattice as the first one turn clockwise, and so on: The whole plane is strictly coupled and the only degree of freedom is the action on first wheel. Thus the magnetic structure of a plane can be described by a single in-plane angle and in the following we use the phase factor $\varphi$ of the $Er^{3+}$ ion at the position $0, y, 0$ for this purpose. Figures 7 and 8 show three situations for different in-plane angles which correspond to the structures of highest symmetry.

In Figure 7 the magnetic unit cell in the *a*-*b* plane is shown. The **k**-vector $(2/3, 0, -1/12)$ determines the spatial modulation of the phase factor $\varphi$ to have a periodicity of $1.5a$ and $12c$. Due to the C-centering of the magnetic structure the *a*-axis has to be tripled to obtain a rectangular translation cell in the *a*-*b* plane. Alternatively, a pseudo hexagonal, primitive unit cell can be chosen with a length of $1.5a$. Accordingly, in Figure 8 only this smaller part of the magnetic structure is shown.

The three-dimensional (3D) magnetic structure of $ErCl_3$ is determined by the stacking of the honeycomb layers. Within a single layer, the $Er^{3+}$ ions are situated on pseudo threefold axes. They have $3n$ ($n$ being an integer number) nearly equidistant, intralayer neighbors which belong to the same magnetic sublattice for each distance. The layer stacking breaks this pseudo threefold symmetry, and in the adjacent planes one out of three nearly equidistant positions belongs to sublattice 1, one to sublattice 2, and the third one is unoccupied, *i.e.* the center of a honeycomb hexagon, see Figure 9. According to the **k**-vector the magnetic moments are rotated by 30° from layer to layer, *i.e.* the sublattice related to $\varphi$ by $-30°$ and that of $(180° - \varphi)$ by 30° along the *c*-axis. The three situations shown in Figures 7 and 8 thus not only display the magnetic structures of one layer for different in-plane angles of 0°, −30°, and −60° but also the stacking sequence of three adjacent layers along the *c*-axis. The 3D

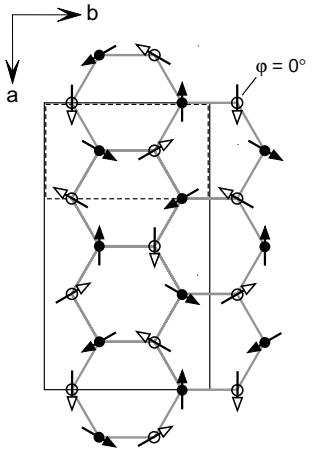


**Fig. 7.** Orientation of the magnetic moments of $ErCl_3$ in the *a*-*b* plane. The open symbols belong to the 0, $y$, 0 magnetic sublattice, *i.e.* that with a clockwise rotation along the *c*-axis, the full symbols belong to the 0, $-y$, 0 sublattice with the counter-clockwise rotation. The magnetic unit cell in the *a*-*b* plane is marked by the full line, the crystallographic unit cell by the dashed one, *cf.* Figure 2.

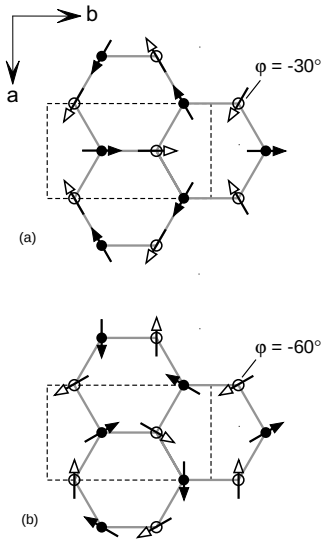


**Fig. 8.** Orientation of the magnetic moments of $ErCl_3$ on the honeycomb net for different in-plane rotation angles. The open and full symbols refer to the two magnetic sublattices. The sequence $\varphi = 0°$ (Fig. 7), $-30°$ (Fig. 8a), and $-60°$ (Fig. 8b) also demonstrates the layer stacking along the *c*-axis. The crystallographic unit cell in the *a*-*b* plane is marked by the dashed line.

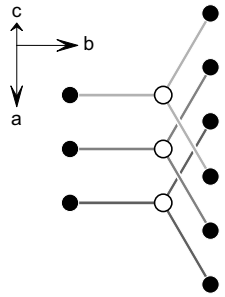


**Fig. 9.** View perpendicular to the *a*-*b* plane of the coordination geometry of $Er^{3+}$ by in-plane and adjacent-plane $Er^{3+}$ neighbors. The full and open symbols refer to the two magnetic sublattices.

magnetic structure of $ErCl_3$ can be described in terms of left- and right-handed helices along the *c*-axis for the $\varphi$ and $(180° - \varphi)$ sublattices, respectively. The magnetic moments are oriented in the *a*-*b* plane and their angles with the *c*-axis vary from $\beta$ to $180° - \beta$ according to the monoclinic crystal symmetry. The shortest interlayer Er-Er distance corresponds to the lattice constant $c = 6.3$ Å. The interlayer magnetic interactions determine the 3D magnetic structure. Based on the crystal structure we expect them to be much weaker than the intralayer neighbor interaction. This view is supported by the fact that in $ErBr_3$ and $ErI_3$ the intralayer spin arrangement is the same as in $ErCl_3$, but the correlation along the *c*-axis is different. The description of the magnetic structure of $ErCl_3$ as quasi 2D is thus appropriate. We are presently in the process of determining the relevant intralayer and interlayer interaction parameters in $ErBr_3$ by inelastic neutron scattering.

The Er site symmetry .2. in $ErCl_3$, *i.e.* a twofold axis parallel to the *b*-axis, is lower than that of ..3 in $ErBr_3$ and $ErI_3$ where the threefold symmetry of the honeycomb layers is preserved in the 3D lattice. This has the remarkable consequence that only $ErCl_3$ shows a long-range 3D magnetic order due to its low symmetry, whereas in $ErBr_3$ and $ErI_3$ the correlation length along the *c*-axis is only 15 Å [4].

The magnetic structure of $ErCl_3$ is described by a model with the amplitude of the ordered moment $\mu_0$ as the only parameter, see Table 3. The components $\mu_x$ and $\mu_y$ are not *a priori* coupled by symmetry. Individual refinement results in $\mu_x = 3.2(6)\mu_B$, $\mu_y = 3.1(2)\mu_B$ and $\mu_z = -0.7(9)\mu_B$. Within error limits $\mu_x$ and $\mu_y$ are equal and $\mu_z$ is zero. Accordingly we set $\mu_x = \mu_y$ and $\mu_z = 0$ to reduce the number of variables. In $ErBr_3$ and $ErI_3$ the structures are rhombohedral, and $\mu_x = \mu_y$ and $\mu_z = 0$ are given by symmetry. In the title compound $ErCl_3$ the data are compatible with these restrictions, but very small deviations cannot be ruled out.

The orientation of the magnetic moments in the *a*-*b* plane is in agreement with magnetic susceptibility measurements [1]. At the ordering temperature the susceptibility parallel to the layer was measured to be six times that perpendicular to it. The ordering temperature of 307 mK determined from the magnetic susceptibility is lower than that of 350(5) mK determined from neutron diffraction. We ascribe this to the inherent difficulty of calibration in this temperature range. The claim of a ferromagnetic or canted antiferromagnetic structure with a net moment could not be confirmed. We find a purely antiferromagnetic structure.

For the Kondo system $UNi_4B$ [14] a magnetic structure with features similar to those of $ErCl_3$ was reported. $UNi_4B$ has no layer structure and the uranium atoms form a triangular lattice with three sublattices in the magnetically ordered state. The magnetic moments of two sublattices are ordered, as shown for $\varphi = 0°$ in Figure 7, but the third sublattice remains paramagnetic. The position of this third sublattice corresponds to the unoccupied centers of the honeycomb hexagons in $ErCl_3$. In contrast to $ErCl_3$, the diffraction pattern of $UNi_4B$ was reported to depend on a rotation of the magnetic moments within the layer. Furthermore, the magnetic interactions in this metallic compound with small magnetic moments and short U-U distances have a completely different physical origin to the insulating $ErCl_3$ with large magnetic moments and long Er-Er distances.

Several transition-metal compounds exhibit honeycomb structures comparable to that of $ErCl_3$, *e.g.* $MPX_3$ with M = Mn and Fe, and X = S [15,16] and Se [17], $BaNi_2(PO_4)_2$ [18,19], and $BaCo_2(AsO_4)_2$ [20]. Due to the larger radial extension of $3d$ electrons with respect to $4f$ electrons the magnetic interactions in the transition metal compounds are much stronger than in the erbium compounds. However, all the mentioned compounds show collinear spin arrangements except $BaCo_2(AsO_4)_2$ which has complicate, magnetic-field dependent, helical structures. $MnPS_3$ and $FePS_3$ crystallize in the same space group C2/m with the magnetic ions at the same site ($4g$) as $ErCl_3$, but the spins are oriented perpendicular to the honeycomb layers. The Néel temperatures are $T_N = 78$ K and 120 K for the Mn and Fe compound, respectively. This distinctly different behavior of the transition-metal compounds is due to the different electronic properties of $3d$ and $4f$ ions in a crystal environment.

A honeycomb net can be decomposed in two triangular nets, as mentioned above. On single triangular nets a 120° antiferromagnetic coupling with in-plane spin orientation was observed in several compounds, *e.g.* $CsCuCl_3$ [21,22], $AVX_3$ (A = Rb, Cs, $N(CD_3)_4$; X = Cl, Br, I) [23], $CsMnBr_3$ [24], $LiCrS_2$ [25] and $TbGa_2$ [26]. As in $ErCl_3$ the absolute in-plane spin orientation is not fixed for these compounds. Magnetic phase diagrams for various 2D layer lattices were theoretically predicted [27,28]. It was shown that helical spin arrangements can occur on triangular and honeycomb nets due to third-nearest neighbor interactions. The 120° antiferromagnetic structure is one possible ground state on a triangular lattice, but it was not predicted for a honeycomb lattice. It was further shown that the 120° antiferromagnetic coupling on a triangular net leads to two ground state patterns with different helicities [29,30]. Their characteristic feature is a triangle with all three spins pointing towards the center or away from the center, respectively. The honeycomb

lattice in $ErCl_3$ is composed of triangular nets of both these helicities depicted by open and filled symbols, respectively, in Figure 8a. In contrast to a single triangular lattice, the in-plane orientation of the spins of each sublattice is no longer arbitrary for $ErCl_3$, but coupled for the two sublattices: in-plane angles $\varphi$ and $180° - \varphi$, respectively.

In insulating rare-earth compounds like $ErCl_3$ magnetic interactions can be either exchange and/or magnetic dipole interactions. Few magnetic structures of rare-earth compounds comparable to $ErCl_3$ have been determined, *e.g.* $GdCl_3$ [31], $MCl_3 \times 6\ H_2O$ with M = Er and Dy [32], $M(OH)_3$ with M = Ho, Dy [33] and Tb [34]. In all these examples the magnetic ordering has been ascribed to dominant magnetic dipole interactions. At very low temperatures, hyperfine interactions between the electronic magnetic moments and the nuclear spins may become important, too. For $Ho(OH)_3$ and $Tb(OH)_3$ there are relevant hyperfine contributions to the specific heat below 1 K. For $MCl_3 \times 6\ H_2O$ with M = Dy and Er as well as for $ErBr_3$ small hyperfine contributions were observed below 0.1 K. Based on the neutron diffraction data presented here we are not able to determine which of the above mentioned interactions are responsible for the order in $ErCl_3$. Information about the intralayer and interlayer coupling parameters either from caloric measurements or inelastic neutron scattering together with the saturation moment $\mu_0 = 3.3\mu_B$ per $Er^{3+}$ determined here is required to settle this question.

The temperature dependence of the ordered magnetic moment per $Er^{3+}$ is shown in Figures 5 and 6. Below the Néel temperature $T_N = 350(5)$ mK $ErCl_3$ is in a 3D ordered state, as described above. In the single crystal measurement, as shown in Figure 6, the 3D magnetic neutron intensity occurs as Bragg peaks which exhibit the same peak shape as the nuclear Bragg peaks. On warming up they lose intensity but do not broaden out, *e.g.* along the *c*-axis, as would happen if the correlation between the layers gets lost. The single-crystal peak shape proves the magnetic order to be 3D, at least up to 325 mK. At temperatures higher than $T_N$ short-range order persists up to about 2 K. This short-range order is expected predominantly in-plane according to the $XY$ type anisotropy. The short-range order contributions are visible in the powder data: at 0.5 K about 40% of the sublattice magnetization is still present. It is also visible in the difference diagram 60–485 mK shown in Figure 3. The broad, short-range order intensity between $2\theta = 8°$ and 22° at 485 mK causes the negative dip in the background. The single-crystal data contain no hint for short-range order. The short-range contributions disappear in the background due their limited dimensionality and correlation length. Above 2 K $ErCl_3$ is paramagnetic and the susceptibility follows the Curie-Weis law [1].

From the temperature dependence of the single-crystal $(-2/3, 0, 1/12)$ magnetic Bragg peak intensity a critical exponent $\beta = 0.23(2)$ was derived. $\beta$ primarily reflects the dimensionality of the interactions. It is in good agreement with values of other quasi-2D systems with $XY$ or anisotropic Heisenberg type interactions [35] where the weak interlayer interactions, present in real systems, give rise to 3D order. A value of $\beta = 0.25$ was derived by Monte Carlo simulations for a Heisenberg antiferromagnet on a layered triangular lattice [36].

The ordered magnetic moment at saturation of $\mu_0 = 3.3\mu_B$ per $Er^{3+}$ in $ErCl_3$ is strongly reduced from the free ion value of $gJ = 9\mu_B$ for the $^4I_{15/2}$ ground state. The crystal field splits the ground state into eight Kramers doublets with an overall splitting of 292 $cm^{-1}$ as has been determined for $Er^{3+}$ in $YCl_3$ [37]. The lowest doublet is separated by 22 $cm^{-1}$ from the next higher one. Thus only the lowest doublet is populated at the ordering temperature. Inelastic neutron measurements are planned in order to obtain wavefunctions for the energy levels from which the magnetic moments can be calculated. Proceeding down the halide series the crystal field interactions and thus the quenching of the magnetic moment decrease. This leads to increased ordered magnetic moments of $4.7\mu_B$ and $5.5\mu_B$ per $Er^{3+}$ at saturation for $ErBr_3$ and $ErI_3$ [4], respectively. $ErF_3$ on the other hand has an ordered magnetic moment of $6.6\mu_B/Er^{3+}$ at saturation [5]. But it cannot be compared directly to $ErCl_3$ because of its different crystal structure.

In conclusion, at very low temperatures $ErCl_3$ shows interesting magnetic effects due to its layer-type crystal structure with dominant intralayer and weak interlayer magnetic interactions. A new type of magnetic structure results with an infinite degree of freedom for the orientation of the moments in the *a*-*b* plane. As for $ErBr_3$ and $ErI_3$ the two $Er^{3+}$ sublattices can be rotated about any arbitrary angle, one left-handed and the other one right-handed, to yield indistinguishable diffraction patterns. The weak interlayer interactions lead to a 3D magnetic order for $ErCl_3$, whereas the different geometrical stacking of the layers in $ErBr_3$ and $ErI_3$ gives rise to disorder in the magnetic stacking. As a result only short range 3D magnetic order occurs in the bromide and iodide [4]. The identical intralayer spin arrangement and the dissimilar 3D magnetic order of the layer-type erbium trihalides can thus nicely be correlated with their crystallographic structures.

The authors want to thank H.-B. Braun and B. Roessli, PSI, for stimulating discussions. The expert operation of the dilution cryostats by S. Pujol, ILL, H. Schneider and M. Meissner, HMI, was crucial for the success of the neutron-diffraction experiments. Financial support of the Swiss National Science Foundation is gratefully acknowledged.

## References

1. C.W. Fairall, J.A. Cowen, E. Grabowski, Phys. Lett. A **35**, 405 (1971).
2. K.H. Hellwege, J. Kötzler, G. Weber, Z. Physik **217**, 373 (1968).
3. F. Varsanyi, K. Andres, M. Marezio, J. Chem. Phys. **50**, 5027 (1969).

4. K. Krämer, H.U. Güdel, B. Roessli, P. Fischer, A. Dönni, N. Wada, F. Fauth, M.T. Fernandez-Diaz, T. Hauß, Phys. Rev. B Rapid Comm. **60**, R3724 (1999).
5. K. Krämer, H. Romstedt, H.U. Güdel, P. Fischer, A. Murasik, M.T. Fernandez-Diaz, Eur. J. Solid State Inorg. Chem. **33**, 273 (1996).
6. G. Meyer, Inorg. Synth. **25**, 146 (1989).
7. D.H. Templeton, G.F. Carter, J. Phys. Chem. **58**, 940 (1954).
8. J. Rodriguez-Carvajal, Physica B **192**, 55 (1993).
9. Y.A. Izyumov, V.E. Naish, J. Magn. Magn. Mat. **12**, 239 (1979).
10. E.F. Bertaut, *Spin configurations of ionic structures: Theory and practice,* in *Magnetism*, Vol. III, edited by G.T. Rado, H. Suhl (New York, 1963), p. 151.
11. S.L. Altmann, P. Herzig, *Point-group theory tables* (Oxford University Press Inc., New York, 1994).
12. E.F. Bertaut, Acta Cryst. A **24**, 217 (1968).
13. *Powder diffraction file*, International Centre for Diffraction Data, Newtown Square, PA, USA, Ref. No. [42-987], G. Meyer, (1990).
14. S.A.M. Mentink, A. Drost, G.J. Niewenhuys, E. Frikkee, A.A. Menovsky, J.A. Mydosh, Phys. Rev. Lett. **73**, 1031 (1994).
15. K. Kurosawa, S. Saito, Y. Yamaguchi, J. Phys. Soc. Jpn **52**, 3919 (1983).
16. A.R. Wildes, B. Roessli, B. Lebech, K.W. Godfrey, J. Phys. Cond. Matt. **10**, 6417 (1998).
17. A. Wiedemann, J. Rossat-Mignod, A. Louisy, R. Brec, J. Rouxel, Solid State Com. **40**, 1067 (1981).
18. L.P. Regnault, J. Rossat-Mignod, *Magnetic properties of Layered Transition Metal Compounds*, edited by L.J. de Jongh (Kluwer Academic, 1990).
19. L.P. Regnault, J. Rossat-Mignod, J.Y. Henry, R. Pynn, D. Petitgrand, *Magnetic Excitations in the Quasi-2d Planar Magnets $BaM_2(XO_4)_2$ (M=Co, Ni; X=P, As),* in *Magnetic Excitations and Fluctuations*, edited by S.W. Lovesey, U. Balucani, F. Borsa, V. Tognetti (Springer-Verlag, 1984).
20. L.P. Regnault, J. Rossat-Mignod, J. Magn. Magn. Mat. **14**, 194 (1979).
21. H.B. Weber, T. Werner, J. Wosnitza, H.v. Löhneysen, U. Schotte, Phys. Rev. B **54**, 15924 (1996).
22. M. Hiroi, M. Sera, H. Nojiri, N. Kobayashi, M. Motokawa, H. Tanaka, Physica B **284-288**, 1605 (2000).
23. A. Hauser, U. Falk, P. Fischer, H.U. Güdel, J. Solid State Chem. **56**, 343 (1985).
24. M. Eibschütz, R.C. Sherwood, F.S.L. Hsu, D.E. Cox, AIP Conf. Proc. **10**, 684 (1972).
25. B. van Laar, D.J.W. Ijdo, J. Solid State Chem. **3**, 590 (1971).
26. H. Asmat, D. Grignoux, R. Lemaire, Physica B **86-88**, 185 (1977).
27. E. Rastelli, A. Tassi, L. Reatto, Physica, B **97**, 1 (1979).
28. E. Rastelli, A. Tassi, L. Reatto, J. Magn. Magn. Mat. **15-18**, 357 (1980).
29. D.P. Landau, J. Appl. Phys. **73**, 6091 (1993).
30. D.H. Lee, J.D. Joannopoulos, J.W. Negele, D.P. Landau, Phys. Rev. B **33**, 450 (1986).
31. J. Kötzler, W. Scheithe, K. Knorr, W.B. Yelon, J. Phys. C **9**, 1291 (1976).
32. E. Lagendijk, W.J. Huiskamp, Physica **65**, 118 (1973).
33. C.A. Catanese, H.E. Meissner, Phys. Rev. B **8**, 2060 (1973).
34. C.A. Catanese, A.T. Skjeltorp, H.E. Meissner, W.P. Wolf, Phys. Rev. B **8**, 4223 (1973).
35. S.T. Bramwell, P.C.W. Holdsworth, J. Appl. Phys. **73**, 6096 (1993).
36. H. Kawamura, J. Phys. Soc. Jpn **54**, 3220 (1985).
37. J.W. Rakestraw, G.H. Dieke, J. Chem. Phys. **42**, 873 (1965).